

Quantum process tomography of a Mølmer-Sørensen gate via a global beam

Holly N Tinkey¹, Adam M Meier¹, Craig R Clark¹,
Christopher M Seck², and Kenton R Brown¹

¹ Georgia Tech Research Institute, Atlanta, GA, United States of America

² Oak Ridge National Laboratory, Oak Ridge, TN, United States of America

E-mail: holly.tinkey@gtri.gatech.edu

January 2021

Abstract. We present a framework for quantum process tomography of two-ion interactions that leverages modulations of the trapping potential and composite pulses from a global laser beam to achieve individual-ion addressing. Tomographic analysis of identity and delay processes reveals dominant error contributions from laser decoherence and slow qubit frequency drift during the tomography experiment. We use this framework on two co-trapped $^{40}\text{Ca}^+$ ions to analyze both an optimized and an overpowered Mølmer-Sørensen gate and to compare the results of this analysis to a less informative Bell-state tomography measurement and to predictions based on a simplified noise model. These results show that the technique is effective for the characterization of two-ion quantum processes and for the extraction of meaningful information about the errors present in the system. The experimental convenience of this method will allow for more widespread use of process tomography for characterizing entangling gates in trapped-ion systems.

Keywords: quantum computing, trapped ions, quantum process tomography

1. Introduction

Substantial quantum computations in a system of real utility will involve long sequences of one- and two-qubit gate operations [1], so a thorough characterization of specific gates is important for predicting how they will behave in such sequences and how experimental errors will propagate [2]. The most widely used method for quantifying two-qubit entangling gate performance in systems of trapped ions is to use the gate to create a Bell state and then to analyze this state with quantum state tomography (“Bell-state tomography”). This technique is popular because it requires only the gate interaction and a global one-qubit gate for analysis [3, 4]. Bell-state tomography measures how well the experimentally produced state matches an intended entangled state, consolidating coherent and stochastic errors into a single number [5]. However,

it falls short of providing a comprehensive description of the quantum process useful for identifying sources of error or for modeling gate performance in the context of more complex sequences.

Quantum process tomography (QPT) is a characterization technique that generates a comprehensive description of a quantum process through representation as a linear mapping of density matrices. The output of QPT is a process matrix that decomposes the full dynamics of an experimentally implemented quantum operation, including decoherence and systematic errors, in terms of a weighted sum over a basis of operators [6, 7]. It has been used to characterize one-qubit and two-qubit quantum gates in a variety of physical qubit platforms [8, 9, 10, 11, 12, 13, 14, 15], but the cumbersome experimental demands and time costs have limited its widespread use as a diagnostic tool in trapped-ion systems. Gathering the necessary data in a reasonable timeframe and with enough precision to extract meaningful information about gate errors requires high-fidelity one-qubit rotations that take a short duration in comparison to the gate of interest.

In this paper, we present a framework for performing QPT on two co-trapped ions that alleviates the time, ion-transport, and hardware constraints of other techniques. We achieve single-ion addressing through a method involving modulations of the ions' confining potential, as previously demonstrated by Seck *et al.* [16], but improved here to reduce the impact on ion temperatures. Section 2 provides a brief summary of the mathematical formulation of QPT and of the challenges of performing QPT with trapped-ion chains. Section 3 contains details about the experimental apparatus, the potential-modulation ion-addressing method, and our QPT framework. In Section 4, we discuss process tomography of identity and delay processes, analyze baseline errors in the QPT experiment, and construct the process matrices of both an optimized and an overpowered Mølmer-Sørensen (MS) gate [17]. The Appendix describes our reduction of heating induced by potential modulations through a finer sampling of the electrode potential waveforms.

2. QPT with Trapped Ions

QPT is a method for estimating the quantum transfer function of a process that evolves a quantum mechanical state [6]. Any quantum process can be expressed as a completely positive linear map \mathcal{E} that acts upon an appropriately-sized input density matrix ρ_{in} to produce ρ_{out} : $\mathcal{E}(\rho_{in}) = \rho_{out}$. Mathematically, the map \mathcal{E} can be expressed using an operator sum representation over a set of Kraus operators with complex weights [18]. For a fixed set of Kraus operators, typically constructed from tensor products of I , X , Y and Z Pauli operators for the qubits, a quantum process can be fully described by the complex weights stored in the process matrix (often referred to by the Greek letter χ) [19]. For a process acting on n qubits, the $4^n \times 4^n$ elements of χ provide a complete mathematical picture of the quantum process under study, which will include not only unitary quantum logic gate operations but also environmental effects such as

decoherence and systematic errors such as inaccurate gate calibrations [20].

QPT experiments involve initializing n qubits into 4^n input states, acting on these states with the quantum process, and performing state tomography on the resulting output states. State tomography of each state can be performed using 4^n different measurement settings, each of which can be implemented by performing a different non-entangling gate on the qubits prior to standard (Z-basis) measurement of the qubits. In this work, we use maximum likelihood estimation (MLE) to derive the most probable process matrix given our experimentally measured populations, thereby avoiding unphysical process matrices that can be obtained through the simpler technique of matrix inversion when noise is present in the measurements [21, 22, 23, 24]. After constructing χ , it is possible to compare the experimental process to the ideal quantum gate, to calculate the process fidelity, and to identify errors in the process.

To date, experimental groups demonstrating tomography on entangling gates for trapped ions have leveraged several different techniques to implement the required individual addressing of the ions; Riebe *et al.* characterized cNOT gate sequences with and without pulse shaping using tightly focused beams to produce single-ion rotations, a technique which produced crosstalk effects on the neighboring ions [12]. Herold *et al.* also studied a cNOT gate sequence using narrowly focused beams to provide cascading pairwise addressing for single-ion control, but the cascaded transport time and crosstalk effects produced a 5% error baseline on their two-ion QPT experiments [13]. Navon *et al.* investigated the performance of concatenated MS gates to extract an error per gate by using a micromotion-induced transition for individual addressing; this method is susceptible to drift of the background electric field that contributed to an error of 5(2)% for an identity operation [14]. A study by Hanneke *et al.* relied on separating ions from larger chains and on sympathetic cooling with a second ion species to perform individual rotations, a technique which is time intensive and requires additional hardware to support the second ion species [15].

The difficulty in performing fast, high-fidelity individual-ion addressing has been a barrier to more widespread adoption of QPT in trapped-ion systems, because QPT analysis typically assumes perfect state preparation and detection. The ideal single-ion rotation should be high fidelity and fast with respect to the duration of the gate being characterized so that analysis of the gate is not obscured by individual addressing errors or sources of environmental decoherence. The potential modulation method we utilize for single-ion addressing provides this critical combination of fidelity and speed. We incorporate the method into an experimental framework to demonstrate QPT analysis of an entangling MS gate and observe a lower baseline error for an identity process than has been achieved with other individual addressing methods. Implementing this method requires simple hardware to control the trap electrode voltages and the phase of a single global beam.

3. Experiment

For these experiments, two $^{40}\text{Ca}^+$ ions are confined with a surface-electrode linear Paul trap [16, 25]. Radial confinement is provided by an RF potential at 56.4 MHz (peak voltage ≈ 176 V) that traps the ions 58 μm above the trap surface. An arbitrary waveform generator (AWG) with a 5 ns sampling rate applies synchronized potentials to 42 segmented electrodes along the trap axis and implements waveforms for ion transport and confinement modulation. The center-of-mass (COM) and breathing mode (BM) secular frequencies are $\omega_{\text{COM}} = 2\pi \times 1.41$ MHz and $\omega_{\text{BM}} = 2\pi \times 2.45$ MHz respectively. Qubit information is stored in the $|S\rangle \equiv |S_{1/2}, m_j = -1/2\rangle$ ground state and metastable $|D\rangle \equiv |D_{5/2}, m_j = -1/2\rangle$ state, and transitions between these states are achieved with a narrow-linewidth 729 nm beam oriented at 45° to the trap axis and illuminating both ions. The ion states are measured by illuminating them with light near 397 nm and monitoring the resulting fluorescence; we can distinguish between the two-ion bright state ($|SS\rangle$), the one-ion bright states (combinations of $|SD\rangle$ and $|DS\rangle$), and the dark state ($|DD\rangle$). Repeating an experiment allows us to estimate the fraction of the final population (P_2, P_1, P_0) in each of these three possible configurations.

We realize individually addressed one-qubit rotations through composite sequences of 729 nm laser pulses and modulations to the confining potential as described in [16]. Here we use two laser pulses and two potential modulations to produce one-qubit rotations on a single ion in 15 μs . For our beam geometry and orientation, increasing the axial confinement to produce center-of-mass frequency $\omega'_{\text{COM}} = 2\pi \times 1.71$ MHz is sufficient to reduce the ion separation by 0.531 nm, creating a differential optical phase shift between the ions of π in the global 729 nm beam. Our previous work with these sequences was limited by significant heating during the potential modulations; here the incorporation of AWGs with a much higher sampling rate allows for faster and smoother potential modulations that reduce this heating (described in the Appendix).

The MS gate under analysis in this work was performed by the simultaneous application of two 729 nm tones at detunings $\pm 2\pi \times 8.3$ kHz from the red and blue breathing-mode motional sidebands of the qubit transition for a duration of 120 μs . The optical intensity is adjusted to produce a maximally entangled state $(|SS\rangle - i|DD\rangle)/\sqrt{2}$. We estimate the Bell-state fidelity of the gate using the results of two experiments: a measurement of the P_0 and P_2 populations after the gate is performed, and a measurement of the populations as a function of the phase of a final analysis pulse to construct a parity signal with amplitude P_{amp} [26, 27]. The Bell state fidelity for our optimized gate is $F_{\text{BST}} = \frac{1}{2}P_{amp} + \frac{1}{2}(P_0 + P_2) = 96.2(7)\%$.

Our experimental QPT framework incorporates the potential modulation-based single-ion rotations to realize state initialization before the quantum process under analysis and measurement rotations for state tomography after the quantum process. One of four rotations (identity, π and $\frac{\pi}{2}$ rotations about the X axis, and $\frac{\pi}{2}$ about the Y axis) is applied to each ion after initialization in the $|SS\rangle$ state, creating one of 16 input states on which the quantum process will act (ρ_{in}). To characterize the state (ρ_{out})

after the process, one of the same four rotations is applied to each ion to generate one of 16 readout directions. In total we perform 256 different experiments, one for each combination of initialization and measurement settings, and we repeat each of these experiments 500 times to develop statistics.

4. QPT Results and Analysis

For all of the following analyses we use MLE to determine the quantum process χ_{exp} most likely to have generated our experimental data. We calculate the process fidelity $F_p = Tr[\chi_{exp} \cdot \chi_{ideal}]$ through comparison with the expected process χ_{ideal} [12]. We estimate the uncertainty on this fidelity through a resampling of our experimental data based on the statistical uncertainty for each population measurement.

4.1. Identity and Delay Process Tomography

We first apply the QPT experimental framework to an identity (null) operation and to a delay (time-evolution) operation to understand the errors present in our system and to examine how these errors accumulate during the tomography procedure. The experiment for the identity operation consists of performing the single-ion initialization and measurement rotations with no intermediate interaction or delay. In the absence of decoherence and systematic experimental errors, all of the weight for this process matrix (χ_{Id} , Fig. 1 (a) and (b)) would fall into the II-II element (i.e., the Kraus operator element that acts on ρ_{in} as $(I_1 \otimes I_2)\rho_{in}(I_1 \otimes I_2)$). Here we determine the fidelity is $F_p = 97.7(3)\%$.

The experiment for the delay operation consists of initialization and measurement rotations separated by a 120 μ s delay to mimic the duration of our MS gate. QPT analysis here produces a process matrix (χ_{Del} , Fig. 1 (c) and (d)) with process fidelity 93.6(5)% exhibiting stronger diagonal IZ and ZI process matrix components compared to the identity. To better understand the observed process matrices, we performed Monte-Carlo simulations of these experiments incorporating a few suspected error sources: laser phase noise, qubit and laser frequency drift, qubit frequency miscalibration, and individual-addressing pulse phase and time miscalibrations. We estimated the magnitude of qubit and laser frequency drift from repeated measurements of the qubit frequency over the same interval as the QPT experiment (30 minutes). Miscalibration values for qubit frequency, pulse time, and pulse phase were given by uncertainties in the calibration fits. Random phase noise from the laser was taken from a Gaussian distribution with a width proportional to the time between each laser pulse of the experiment.

We find that miscalibrations and errors in the individual addressing method are not responsible for the dominant errors present in the process matrices for the identity or delay. Incorrectly applied phases, pulse times, or qubit frequency add coherently over multiple single-ion addressing composite pulses and manifest as correlated errors with equal amplitudes for errors on each ion (e.g. corresponding IX and XI components

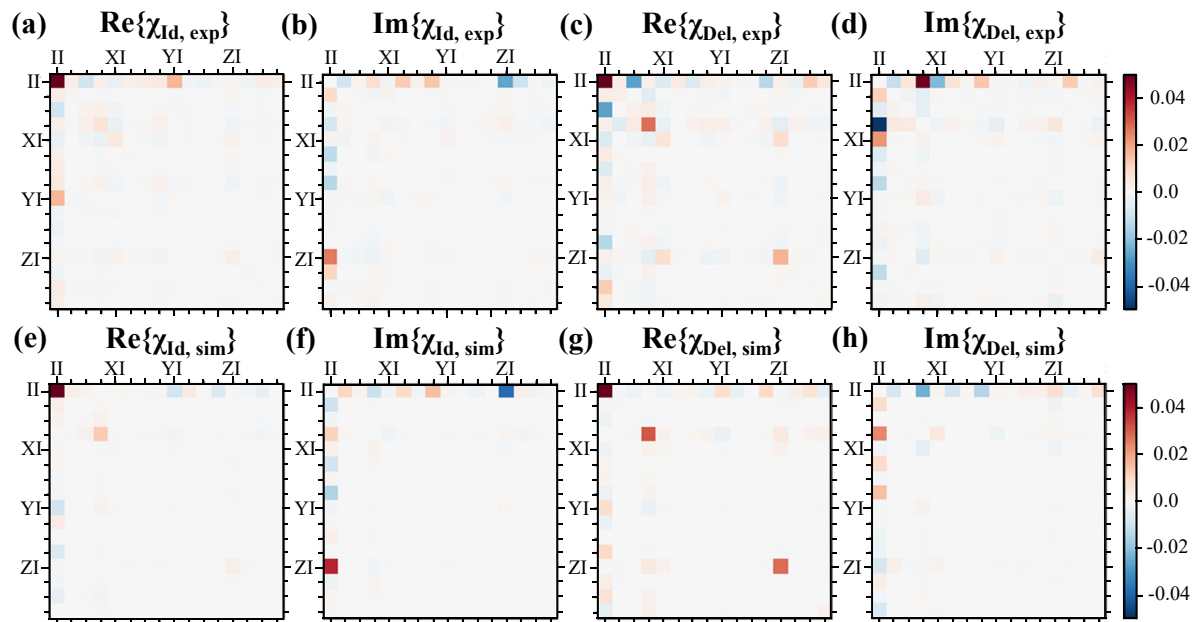


Figure 1. (a) Real and (b) imaginary amplitudes of the process matrix $\chi_{\text{Id,exp}}$ constructed from experimental data of an identity operation with error 2.3(3)%. Elements of χ are in the basis $\sigma_i^{\text{ion}1} \otimes \sigma_j^{\text{ion}2}$ where $\sigma_{I,X,Y,Z}$ are denoted with $I, X, Y,$ and Z and are in order $II, IX, IY, IZ, XI, XX, \dots ZZ$. (c) Real and (d) imaginary amplitudes of a process matrix $\chi_{\text{Del,exp}}$ constructed from experimental data of a $120 \mu\text{s}$ delay with error 6.4(5)%. (e) Real and (f) imaginary amplitudes of a process matrix $\chi_{\text{Id,sim}}$ from simulated QPT data of an identity operation with error 2.4(4)%. (g) Real and (h) imaginary amplitudes of a process matrix $\chi_{\text{Del,sim}}$ of simulated data of a $120 \mu\text{s}$ delay with error 6.5(5)%. The II-II elements of the $\text{Re}\{\chi\}$ are saturated in these figures to highlight error processes.

would be equal and associated with correlated XX components). On the contrary, the process matrices contain imbalanced components for processes on each ion (see the real YI-II components in Fig. 1(a) or imaginary ZI-II components in Fig. 1(d) that do not contain corresponding errors on the other ion). Dominant individual addressing errors would also not account for the difference in overall error between the identity and delay processes. We find that random phase noise during the individual addressing sequences as well as slow frequency drifts can account for the magnitude of the errors in the identity and delay processes and qualitatively reproduce the dominant error components of χ in each case. These errors create predominantly uncorrelated Z-type errors on each ion separately; this manifests in the process matrices as real diagonal IZ-IZ and ZI-ZI components (see Fig. 1 (a) and (c)) and as imaginary IZ-II and ZI-II components (see Fig. 1 (b) and (d)) that can grow in magnitude over delay times in a manner consistent with the process matrices we observe. Laser coherence and qubit frequency drift are well-known sources of error in trapped-ion QPT experiments [12, 28]; however, the method of individual addressing employed here still results in a better baseline identity process fidelity than has been achieved using other methods [13, 14]).

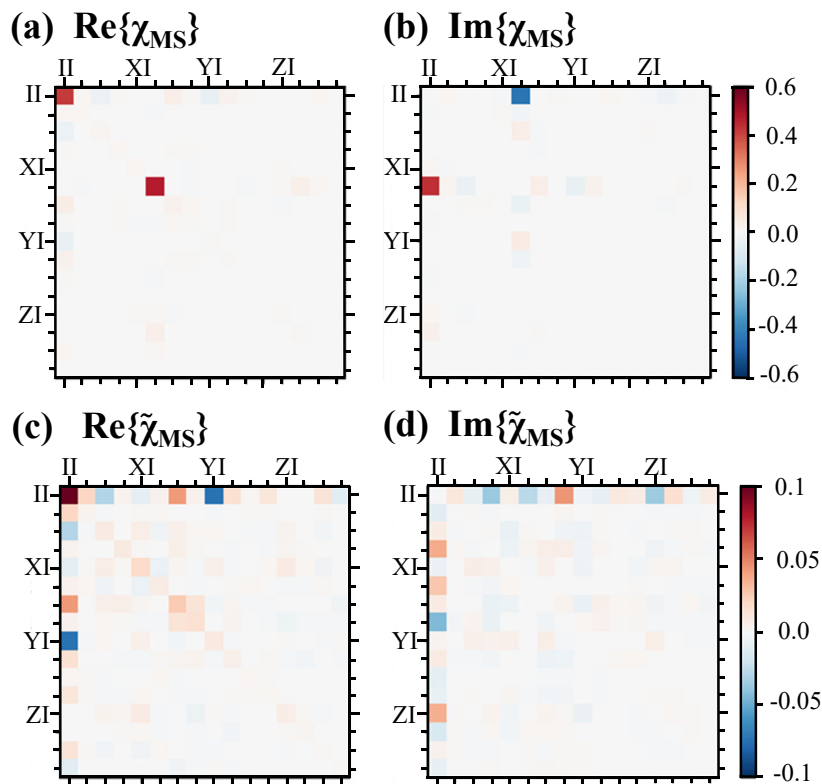


Figure 2. (a) Real and (b) imaginary components of the process matrix χ_{MS} of an experimentally implemented MS gate with $F_p = 88.1(5)\%$. (c) Real and (d) imaginary components of the error process matrix $\tilde{\chi}_{MS}$ for the MS gate. The weight of the II-II real entry is 88.1% and has been saturated in the image to show the other errors more clearly.

4.2. MS Gate Process Tomography

The propagator for the MS gate can be written as $\exp\{-i\frac{\pi}{4}X_1X_2\} = (I_1I_2 - iX_1X_2)/\sqrt{2}$, so that the corresponding χ process matrix contains four nonzero elements: $\chi_{II,II} = \chi_{XX,XX}$ and $\chi_{II,XX} = -\chi_{XX,II}$ [14]. The experimentally determined process matrix for our MS gate (χ_{MS} , Fig. 2 (a) and (b)) closely agrees with these predicted values, although there is some disagreement due to the baseline errors already explored in Section 4.1 as well as to errors inherent in the gate implementation. Here we calculate a process fidelity $F_p = 88.1(5)\%$. This 11.9(5)% deviation from the ideal gate can be understood roughly as a combination of the 6.4% baseline error measured for the delay operation and the 3.8% MS gate error determined through Bell-state tomography (Section 3). These results may be recast in the form of a process error matrix for the MS gate $\tilde{\chi}_{MS}$ so that the measured quantum process becomes a composition of the ideal unitary evolution and the error process captured by $\tilde{\chi}_{MS}$ [29, 30]. The II-II entry in the error matrix (Fig. 2 (c) and (d)) is equal to F_p ; while all other entries indicate errors occurring in addition to the ideal process. This representation makes it easier to visualize errors that might otherwise be overshadowed by the ideal behavior in the usual process matrix.

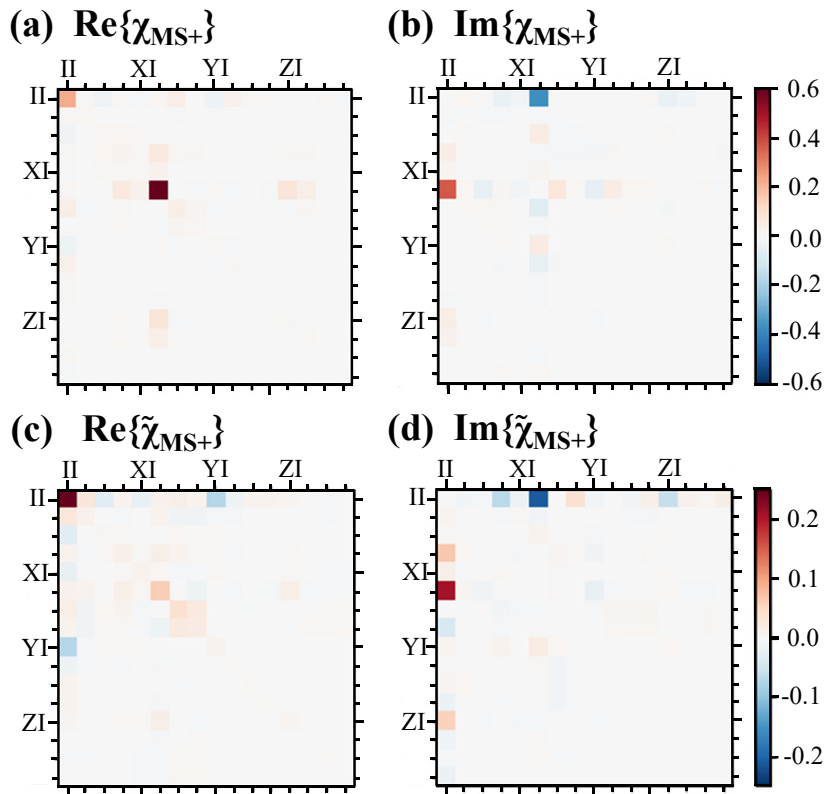


Figure 3. (a)Real and (b)imaginary components of the process matrix χ_{MS+} for an overpowered MS gate with $F_p = 81.5(6)\%$. (c)Real and (d)imaginary components of the process error matrix $\tilde{\chi}_{MS+}$ for the overpowered MS gate. The weight of the II-II real entry is 81.5% and has been saturated in the image to show the other errors more clearly.

To emphasize the diagnostic power of QPT, we intentionally increase the RF power driving an acousto-optic modulator in the MS gate beam path by 1.5 dB. This results in a 32% increase in optical intensity at the ions (smaller than the expected 41% increase due to saturation of the AOM response). Bell state tomography of the resulting gate yields a fidelity of $F_{BST} = 90.1(7)\%$ (we would have expected a reduction of 6.3% below the fidelity of the optimally tuned gate, in agreement with the observed decrease), but this analysis provides only limited information about the nature of the additional errors taking place. Process tomography of the overpowered gate (Fig. 3) produces a process matrix χ_{MS+} with imbalanced weights, as expected ($\chi_{II,II} = 0.224$, $\chi_{XX,XX} = 0.638$, $\chi_{XX,II} = 0.012 + 0.370i$, $\chi_{II,XX} = 0.012 - 0.370i$) and a process fidelity of 81.5(6)%. This 6.6(6)% reduction in process fidelity below that of the optimally tuned gate is consistent with the theoretically expected 6.3% decrease, but here the process matrix provides far more information about the nature of the new errors. The corresponding process error matrix $\tilde{\chi}_{MS+}$ clearly shows the dominant XX-II, II-XX, and XX-XX character of these errors.

5. Conclusion

The greatest benefit of performing QPT is the sheer amount of information collected about a gate and the ability to identify prevalent error processes. The process matrix signature of a power miscalibration for an MS gate is demonstrated here, but other common gate errors such as unequal illumination of one ion over another or poor calibration of the red or blue axial sideband frequencies can also be diagnosed through process matrices. Two drawbacks of QPT are the extraneous errors due to the additional one-qubit rotations and its longer experimental duration in comparison to simpler evaluation techniques. Due to the longer duration, various experimental imperfections (e.g. laser noise, slow magnetic field drift) impact the process tomography protocol more than the Bell state tomography protocol, resulting in the fidelity estimated from process tomography being consistently lower than the Bell state fidelity [31]. Bell-state tomography and QPT characterization methods are therefore complementary for diagnosing gate performance, and the adoption of one over the other depends on the specific needs of an experiment.

Quantum process tomography is a powerful technique for comprehensively characterizing quantum operations and diagnosing errors in their experimental implementation. The potential modulation method demonstrated here for realizing single-ion rotations with a global gate beam is an effective method for performing QPT in trapped-ion systems. QPT analysis of identity and delay processes allows us to quantify the effects of laser noise and drift present in our experimental apparatus and to establish a baseline for use of the technique on more interesting two-qubit processes. We are able to reconstruct the process matrix of a two-ion entangling gate and to replicate the expected process errors for an intentionally miscalibrated gate. With this framework in place, it is possible to diagnose and mitigate specific errors in the MS gate, to predict the performance of longer gate sequences, and to study other quantum processes. The low experimental overhead required for this technique will make QPT more accessible to other ion-trapping experiments.

6. Appendix: Reduction of motional heating induced by potential modulations

To produce high-fidelity single-ion rotations for qubit state initialization and measurement during the QPT experiments, we sought to reduce the axial mode heating previously observed in randomized benchmarking experiments of the potential modulation single-ion addressing technique [16]. For that work, the trap electrode voltages were provided by National Instruments 16-bit PXI-6733 digital-to-analog converter (DAC) cards in a PXI-1045 chassis. The large number of cards in use there combined with an idiosyncrasy of the particular computer-chassis interface limited the update speed of the waveform voltages to 25 μ s. To minimize the duration of the single-ion operations, voltages for the potential modulations were changed from initial to final

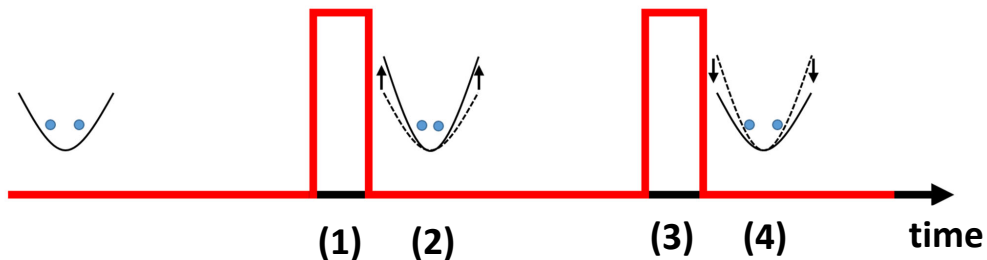


Figure 4. Pulse and potential-modulation sequence for the individual-ion-addressing method. Red lines indicate pulses of the 729 nm laser (steps 1 and 3) and black parabolas indicate configurations of and changes in the confining potential (steps 2 and 4). The interval from the initial laser pulse to the end of the second potential modulation (previously 50 μ s with the PXI-6733 cards) was reduced to 15 μ s with the PXIe-5413 cards.

values in a single update. This ‘snapped’ potential heated the axial motional modes of the ions, and the heating could be reduced but not eliminated through calibration of background electric fields. Errors due to this motional excitation substantially increased for longer sequences of single-ion operations.

To reduce this heating we installed DACs with a faster sampling rate to interpolate more smoothly between initial and final electrode potential values. We chose a system of National Instruments PXIe-5413 AWG cards (5 ns sampling rate) in a PXIe-1084 chassis to supply the trap voltages. This system enables the use of hundreds of interpolation steps between initial and final potential values within a small fraction of the duration previously required by the ‘snapped’ potentials. The complete composite pulse sequence that produces one individually addressed single-ion rotation consists of two laser pulses and two potential modulations, as shown in Fig. 4. Beginning with the ions in an initial confining potential, (1) a single laser pulse ($\pi/2$ pulse for a total composite π rotation or $\pi/4$ pulse for a total composite $\pi/2$ rotation) rotates the states of both ions, (2) the confinement is tightened with a change of electrode voltages thereby changing the ion positions and spacings, (3) a second laser pulse of the same duration as the first but with a different phase completes the rotation on the targeted ion and returns the untargeted ion to its original state, and (4) the confinement is returned to its original value to simplify preparation for the next arbitrary operation.

To measure the heating caused by these potential modulations, we performed Rabi experiments on the axial COM and BM blue motional sidebands after allowing the ions to undergo some number of potential modulation cycles (departure and return to initial voltage values). The resulting two-ion fluorescence curves were fit to a temperature-dependent model to determine the occupation of the motional mode in coherent (\bar{n}_{coh}) and thermal (\bar{n}_{th}) distributions [32, 33]. Fig. 5 shows such fluorescence curves for the COM mode for three different potential modulation cycles. The first ‘null’ waveform (blue) involves no change of the trap confinement and serves as a baseline for the temperature of the mode ($\bar{n}_{\text{th}} = 5.5 \pm 0.4$, $\bar{n}_{\text{coh}} = 0.4 \pm 0.2$). The curve for the ‘snapped’

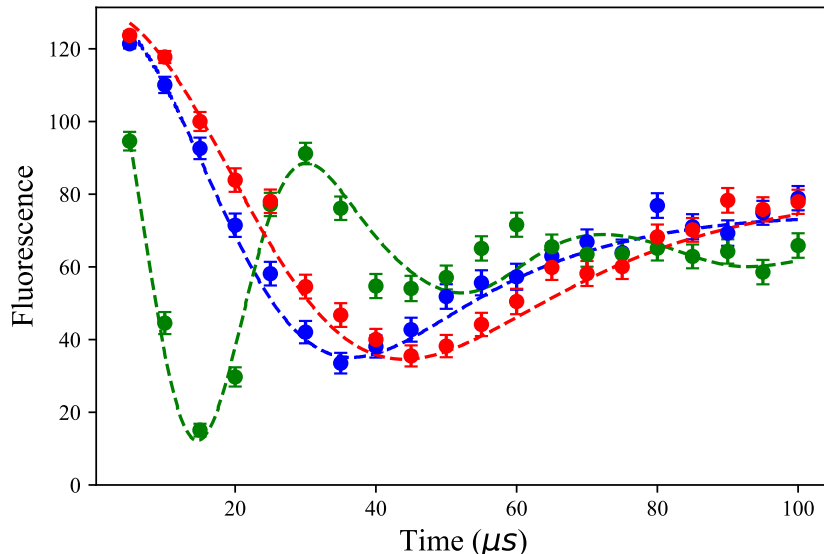


Figure 5. Rabi experiments on the COM blue motional sideband for a null waveform (blue), one cycle of a two-point potential modulation waveform (green), and 100 cycles of a 400-point potential modulation waveform (red).

two-point waveform (green) exhibits faster oscillations indicating a higher temperature ($\bar{n}_{\text{th}} = 31.5 \pm 3.5$, $\bar{n}_{\text{coh}} = 22.4 \pm 1.6$). We chose a waveform with 400 linear interpolation values (red, $\bar{n}_{\text{th}} = 3.5 \pm 0.3$, $\bar{n}_{\text{coh}} = 0.1 \pm 0.1$), which exhibits no heating compared to the null waveform even after 100 potential modulation cycles. Shorter waveforms were also investigated but were found to be less suitable, presumably because the 2 μs duration of the 400-point waveform is already comparable to the timescale set by the 530 kHz corner frequency of our trap electrode filters. We measured no heating of the breathing mode for either of these waveforms. These changes reduced the overall duration of single-ion composite rotations from above 50 μs to 15 μs , allowing us to produce faster sequences with higher fidelity for the QPT experimental framework.

Acknowledgments

Research was sponsored by the Army Research Office under Grant Number W911NF-18-1-0166. The views and conclusions contained in this document are those of the authors and should not be interpreted as representing official policies, either expressed or implied, of the Army Research Office or the U.S. Government. The U.S. Government is authorized to reproduce and distribute reprints for government purposes notwithstanding any copyright notation herein. We would also like to thank Brian Sawyer for developing the fitting routines for analyzing two-ion fluorescence curves and Robin Blume-Kohout for discussions regarding MLE algorithms.

References

- [1] Barenco A, Bennett C H, Cleve R, DiVincenzo D P, Margolus N, Shor P, Sleator T, Smolin J A and Weinfurter H 1995 *Phys. Rev. A* **52** 3457-3467
- [2] Knill E. 2005 *Nature* **434** 39-44
- [3] Benhelm J, Kirchmair G, Roos C F and Blatt R 2008 *Nat. Phys.* **4** 463-466
- [4] Ballance C J, Harty T P, Linke N M, Sepiol M A and Lucas D M 2016 *Phys. Rev. Lett.* **117** 060504
- [5] Bruzewicz C D, Chiaverini J, McConnell R and Sage J M 2019 *Appl. Phys. Rev.* **6** 021314
- [6] Chuang I L and Nielsen M A 1997 *J. Modern Optics* **44** 2455-2467
- [7] Poyatos J F, Cirac J I and Zoller P 1997 *Phys. Rev. Lett.* **78** 390-393
- [8] O'Brien J L, Pryde G J, Gilchrist A, James D F V, Langford N K, Ralph T C and White A G 2004 *Phys. Rev. Lett.* **93** 080502
- [9] Childs A M, Chuang I L and Leung D W 2001 *Phys. Rev. A* **64** 012314
- [10] Neeley M, Ansmann M, Bialczak R C, Hofheinz M, Katz N, Lucero E, O'Connell A, Wang H, Cleland A N and Martinis J M 2008 *Nat. Phys.* **4** 523-526
- [11] Kiesel N, Schmid C, Weber U, Ursin R and Weinfurter H 2005 *Phys. Rev. Lett.* **95** 210505
- [12] Riebe M, Kim K, Schindler P, Monz T, Schmidt P O, Körber T K, Hänsel W, Häffner H, Roos C F and Blatt R 2006 *Phys. Rev. Lett.* **97** 220407
- [13] Herold C D, Fallek S D, Merrill J T, Meier A M, Brown K R, Volin C E and Amini J M 2016 *New J. Phys.* **18** 023048
- [14] Navon N, Akerman N, Kotler S, Glickman Y and Ozeri R 2014 *Phys. Rev. A* **90** 010103
- [15] Hanneke D, Home J P, Jost J D, Amini J M, Leibfried D and Wineland D J 2010 *Nat. Phys.* **6** 13-16
- [16] Seck C M, Meier A M, Merrill J T, Hayden H T, Sawyer B C, Volin C E and Brown K R 2020 *New J. Phys.* **22** 053024
- [17] Sørensen A and Mølmer K 1999 *Phys. Rev. Lett.* **82** 1971-1974
- [18] D'Ariano G M and Lo Presti P 2001 *Phys. Rev. Lett.* **86** 4195-4198
- [19] Kofman A G and Korotkov A N 2009 *Phys. Rev. A* **80** 042103
- [20] Wölk S, Sriarunothai T, Giri G S and Wunderlich C 2019 *New J. Phys.* **21** 013015
- [21] Ježek M, Fiurášek J and Hradil Z 2003 *Phys. Rev. A* **68** 012305
- [22] Blume-Kohout R 2010 *New J. Phys.* **12** 043034
- [23] van Enk S J and Blume-Kohout R 2013 *New J. Phys.* **15** 025024
- [24] Hradil Z, Fiurášek J, Řeháček J and Ježek M 2004 Maximum-Likelihood Methods in Quantum Mechanics *Quantum State Estimation* ed M Paris and J Řeháček (Springer, Berlin, Heidelberg) p 59-112
- [25] Shappert C M, Merrill J T, Brown K R, Amini J M, Volin C E, Doret S C, Hayden H T, Pai C-S, Brown K R and Harter A W 2013 *New J. Phys.* **15** 083053
- [26] Leibfried D, DeMarco B, Meyer V, Lucas D, Barrett M, Britton J, Itano W M, Jelenković B, Langer C, Rosenband T and Wineland D J 2003 *Nature* **422** 412-415
- [27] Akerman N, Navon N, Kotler S, Glickman Y and Ozeri R 2015 *New J. Phys.* **17** 113060
- [28] Wang S X, Labaziewicz K, Ge Y, Shewmon R and Chuang I L 2010 *Phys. Rev. A* **81** 062332
- [29] Dewes A, Ong F R, Schmitt V, Lauro R, Boulant N, Bertet P, Vion D and Esteve D 2012 *Phys. Rev. Lett.* **108** 057002
- [30] Korotkov A N 2013 arXiv:1309.6405
- [31] Gilchrist A, Langford N K and Nielsen M A 2005 *Phys. Rev. A* **71** 062310
- [32] Walther A, Ziesel F, Ruster T, Dawkins S T, Ott K, Hettrich M, Singer K, Schmidt-Kaler F and Poschinger U 2012 *Phys. Rev. Lett.* **109** 080501
- [33] Webster S 2005 *PhD Thesis* St, John's College